

VAOT: Vessel-Aware Optimal Transport for Retinal Fundus Enhancement

Xuanzhao Dong^{1*}, Wenhui Zhu^{1*}, Yujian Xiong¹, Xiwen Chen², Hao Wang², Xin Li¹, Jiajun Cheng¹
Zhipeng Wang³, Shao Tang³, Oana Dumitrascu⁴, Yalin Wang¹

¹Arizona State University, AZ, USA

²Clemson University, SC, USA

³LinkedIn Corporation, CA, USA

⁴Mayo Clinic, AZ, USA

Abstract

Color fundus photography (CFP) is central to diagnosing and monitoring retinal disease, yet its acquisition variability (e.g., illumination changes) often degrades image quality, which motivates robust enhancement methods. Unpaired enhancement pipelines are typically GAN-based, however, they can distort clinically critical vasculature, altering vessel topology and endpoint integrity. Motivated by these structural alterations, we propose Vessel-Aware Optimal Transport (VAOT), a framework that combines an optimal-transport objective with two structure-preserving regularizers: (i) a skeleton-based loss to maintain global vascular connectivity and (ii) an endpoint-aware loss to stabilize local termini. These constraints guide learning in the unpaired setting, reducing noise while preserving vessel structure. Experimental results on synthetic degradation benchmark and downstream evaluations in vessel and lesion segmentation demonstrate the superiority of the proposed methods against several state-of-the-art baselines. The code is available at <https://github.com/Retinal-Research/VAOT>

1. Introduction

Retinal color fundus photography (CFP) is pivotal for diagnosing and monitoring ocular diseases [5, 6, 27–30], but image quality is often degraded by uncontrolled acquisition factors such as variable ambient illumination, motion or focus errors, and operator-induced artifacts. The resulting degradations (e.g., contrast mismatch, nonuniform illumination, and vessel attenuation) compromise the faithful visualization of lesions and vasculature that is essential for conditions like hypertensive retinopathy. Consequently, developing robust enhancement frameworks for low-quality CFP is critical to improving diagnostic reliability and down-

stream analysis [4, 31, 32].

Unpaired algorithms currently dominate CFP enhancement, as small acquisition or implementation variations introduce subtle but pervasive differences across images, making the collection of paired data impractical. These methods typically cast enhancement as unpaired domain translation between low and high quality distributions. For example, OTTGAN [21] formulates a Monge optimal transport (OT) objective within an adversarial framework, avoiding the additional computational overhead of auxiliary structures used by CycleGAN [25] and enabling smoother domain shifts. Nonetheless, a central limitation remains when transferring such methods to retinal imaging, which is preserving clinically salient anatomy. In fact, retinal images contain complex structures (e.g., heterogeneous lesions and fine vascular networks) and GAN-based translators, which are prone to mode collapse and unstable training, can distort vessel topology, attenuate subtle lesions or even bring additional artifacts, ultimately undermining their clinical reliability [4, 20, 31]. This motivates the incorporation of explicit structure-aware constraints to maintain anatomical fidelity during enhancement.

To address these challenges, we propose Vessel-Aware Optimal Transport (VAOT), a novel vessel-aware retinal fundus image enhancement framework with three complementary components. First, we leverage an OT theory to promote stable, smooth distribution shifts in the unpaired setting. Second, to preserve global vascular topology, we introduce a skeleton-based regularizer that treats the one-pixel-wide vessel skeleton as a structural prior and a proxy for anatomical alignment. Third, to refine local geometry, we add an endpoint-aware regularization term in image space that emphasizes small, clinically relevant structures. Our contributions are threefold:

- We introduce VAOT, a vessel-aware retinal fundus enhancement model that improves image quality while preserving diagnostically important vascular structure.

*Contributed equally to this paper.

- We propose a mixed structure-preserving scheme. Specifically, skeleton consistency to maintain global topology and overall vessel layout. Endpoint-aware constraints to align local termini.
- We conduct large-scale experiments on public retinal fundus datasets, showing that VAOT outperform multiply baselines in both denoising performance and preservation of vascular topology.

2. Related Work

2.1. Retinal Fundus Image Enhancement

Early work on retinal fundus image enhancement largely relied on paired supervised or self-supervised formulations. For example, PCE-Net [12] leverages Laplacian-pyramid constraints derived from low-quality inputs to guide enhancement, while GFE-Net [11] and SCR-Net [10] inject frequency cues and synthetic data as additional priors. However, the requirement for paired images limits their scalability and practicality in clinical workflows.

The success of CycleGAN [25] opened a path to unpaired enhancement by introducing a dual-generator architecture with cycle consistency, enabling bidirectional mappings without aligned pairs. However, for CFP enhancement, which is predominantly one-directional (i.e., low to high quality), the auxiliary reverse mapping and extra modules add computational overhead that is often unnecessary. Additionally, building on WGAN-based models [1, 7], subsequent approaches [31, 32] employed optimal-transport (OT) theory to achieve smoother distribution alignment. For instance, context-aware OT [20] uses deep feature spaces (i.e., VGG [13]) to compute contextual losses that approximate Earth Mover’s Distance over representations. Beyond GANs, diffusion-based methods have also shown promise. For example, CUNSB-RFIE [4] learns a Schrödinger Bridge (SB) between image domains by estimating multiply SB couplings across sub-intervals via adversarial training, yielding smooth, probabilistically consistent transformations. However, this method fall behind GANs, as those high-frequency details (e.g., lesion structure) are gradually smoothed out during iterative training.

Despite these advances, preserving clinically salient vasculature remains a core challenge. Many existing methods prioritize image or feature level perceptual alignment and may under-penalize localized topological errors (e.g., breaks, merges and endpoint shifts) in blood vessels. To our knowledge, VAOT is the first unpaired CFP enhancement framework that explicitly targets vascular preservation with complementary constraints at two scales. Specifically, the skeleton-based regularization targets global morphology, while the endpoint-aware regularization emphasize local structural alignment.

2.2. Topology Structure Preservation

Topology preservation has been extensively studied in segmentation, particularly for tubular and curvilinear structures (e.g., retinal vasculature in diabetic retinopathy). For instance, [8] introduce a differentiable loss based on persistent homology that aligns birth–death pairs in persistence diagrams to maintain correct connectivity and cycles, while SkelCon [18] integrates skeletal priors into the segmentation network to better preserve vessel morphology. However, despite this progress in segmentation and delineation, applying topology-preserving objectives to retinal fundus image enhancement remains underexplored. VAOT addresses this gap by coupling enhancement with structure-aware constraints that preserve vascular morphology at both global (i.e., overall skeleton) and local (i.e., endpoint-based window) scales.

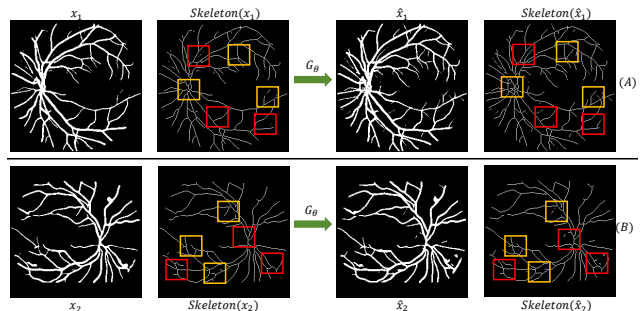


Figure 1. Example (A) and (B) illustration the segmentation mask and corresponding skeleton map (e.g., $Skeleton(x_1)$) for input low quality images (e.g., x_1) and its enhanced counterparts (e.g., \hat{x}_1). The skeleton structure shifts and endpoint modifications are highlight in yellow and red box, respectively. Here, the frozen generator G_θ comes from [32] considering it’s consistent great performance shown in [26], and segmentation network comes from [24]. Algorithms outlined in [19] are used to extract skeleton based on segmentation map. See Sec. 3 for more detailed analysis.

3. Preliminary and Analysis

Let $\mathbf{X} \sim \mathbb{P}_{\mathbf{X}} d\mu$ and $\mathbf{Y} \sim \mathbb{P}_{\mathbf{Y}} d\nu$ denote low-quality and high-quality fundus images, respectively, where μ, ν represent the corresponding measure. We consider two disjoint, unpaired datasets $\mathcal{D}_{\mathbf{X}} = \{x_i\}_{i=1}^{N_{\mathbf{X}}}$ and $\mathcal{D}_{\mathbf{Y}} = \{y_j\}_{j=1}^{N_{\mathbf{Y}}}$ drawn independently from $\mathbb{P}_{\mathbf{X}}$ and $\mathbb{P}_{\mathbf{Y}}$, with no one-to-one correspondences. VAOT, which belong to unpaired enhancement framework, is cast as image-to-image (I2I) translation task. Specifically, it learn a mapping $G_\theta: \mathbf{X} \rightarrow \mathbf{Y}$ such that

$$\hat{x}_i = G_\theta(x_i)$$

matches the target distribution $\mathbb{P}_{\mathbf{Y}}$ while preserving the vascular morphology present in x_i . Here, G_θ is modeled as a generator parameterized by θ . Existing retinal enhancement

frameworks can fail to preserve vascular morphology. In particular, vascular topology may be altered, manifesting as global skeleton changes (e.g., formation or loss of loops) and local endpoint deviations (e.g., spurious branches or vessel breaks). As illustrated in Fig. 1 (A and B), when applied to low-quality inputs, the generator G_θ can introduce artifacts such as false-positive branches (e.g., highlighted in yellow box). The red box marks regions where endpoint conservation is violated (e.g., newly introduced discontinuities). Although visually subtle (i.e., the overall segmentation may appear well preserved), these perturbations substantially degrade structural fidelity and can impair downstream clinical tasks. Directly porting topology-preserving methods from segmentation to enhancement is nontrivial due to mismatched supervision (i.e., explicit mask labels vs. implicit image intensities). As a result, many retinal enhancement methods rely on global regularization (e.g., image- or feature-level perceptual losses) that emphasize overall similarity but under-penalize small structural defects (e.g., terminal-branch breaks or short spurious vessels). The issue is exacerbated when regularizing with segmentation masks, since noisy inputs and imperfect labels can compromise network integrity, making it difficult to distinguish genuine vascular structure from false positives. As a result, hard alignment to such masks may even hinder denoising. This raises a central design question for vessel-aware enhancement:

Given limited and potentially noisy structural cues (e.g., segmentation masks), how can we enforce both global and local vascular morphology preservation during enhancement?

To address these issues, we propose VAOT, which comprises three complementary components detailed in the next section.

4. Method

VAOT comprises three modules: (i) an optimal-transport-based enhancement backbone that induces smooth distribution shifts in the unpaired setting (Sec. 4.1); (ii) Skeleton-Guided global morphology Alignment (SGA), a regularizer designed to preserve global vascular topology using skeleton pseudo-labels (Sec. 4.2); and (iii) Endpoint-based vascular integrity Preservation (EVP), which refines local structure around vessel terminals in image space (Sec. 4.3).

4.1. Image Enhancement Guided by Optimal Transport

As discussed in Sec. 3, the retinal image enhancement problem can be cast as a *Monge’s* optimal transport prob-

lem, denoted as:

$$f^* = \inf_f \int_{\mathbf{X}} C(\mathbf{x}, f(\mathbf{x})) d\mu \quad (1)$$

subject to $f_{\#}\mu = \nu$

Here, f denote a measurable transport map and $C(\cdot, \cdot)$ is a pointwise cost function (e.g., the squared L2 loss). The push forward constraint $f_{\#}\mu = \nu$ ensure that for any measurable set $B \subseteq \mathbf{Y}$, the probability mass of $f^{-1}(B) \subseteq \mathbf{X}$ is preserved.

Following prior works [21, 31, 32], we model Eq. 1 with GAN-style adversarial learning framework, denoted as:

$$\max_{G_\theta} \min_{D_\beta} \lambda_1 \mathbb{E}_{\mathbf{x}}[C(\mathbf{x}, G_\theta(\mathbf{x}))] + \lambda_2 \mathbb{E}_{\mathbf{y}}[C(\mathbf{y}, G_\theta(\mathbf{y}))] + \mathbf{W}_1(\mathbb{P}_{G_\theta(\mathbf{X})}, \mathbb{P}_{\mathbf{Y}}) \quad (2)$$

Specifically, the generator G_θ aims to approximate optimal transport map f^* , while the discriminator D_β serves as a 1-Lipschitz critic estimating the Wasserstein-1 distance between the generated distribution $\mathbb{P}_{G_\theta(\mathbf{X})}$ and the target distribution $\mathbb{P}_{\mathbf{Y}}$. The identity regularization term $C(\mathbf{y}, G_\theta(\mathbf{y}))$ discourages unnecessary changes to already clean images. λ_1 and λ_2 works as balancing parameters. We instantiate cost function C using the Local Quasi-Convex Multi-Scale Structural Similarity Index Measure [2, 22], and we enforce the Lipschitz condition on D_β with the gradient penalty method [7].

However, strong distributional alignment does not by itself ensure preservation of vascular morphology (see example (B) in Fig. 1), even under objectives that emphasize perceptual similarity (e.g., SSIM). Additional mechanisms are needed to encourage both global topology and local structural alignment without compromising denoising performance.

4.2. Skeleton-Guided Global Morphology Alignment

Give a low quality image \mathbf{x} and its enhanced counterpart $\hat{\mathbf{x}}$, we can get the corresponding segmentation likelihoods $S(\mathbf{x})$ and $S(\hat{\mathbf{x}})$ (e.g., after sigmoid operation) from a pretrained vessel segmenter S . However, enforcing topology with these masks is risky, as the noise and artifacts in \mathbf{x} often degrade $S(\mathbf{x})$, so forcing $S(\hat{\mathbf{x}})$ to match $S(\mathbf{x})$ can anchor the generator to noisy labels and conflict with denoising. As shown in Fig. 2, the red box highlight regions where noise affects the results, directly enforcing alignment will encourage G preserve spurious loops.

In contrast, the morphological skeleton $SK(\cdot)$ (e.g., $SK(\mathbf{x})$), which represents vessels as one-pixel-wide centerlines, provides a compact alternative that preserves vascular connectivity and branching while discarding uncertain

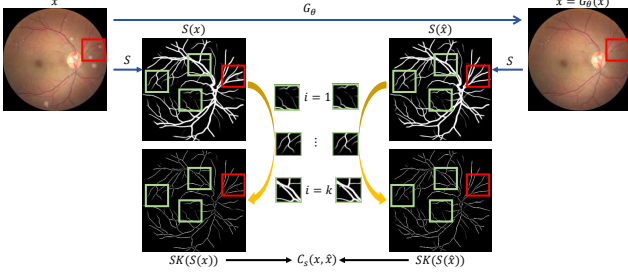


Figure 2. Illustration of the SGA modules. Specifically, given low quality image \mathbf{x} and its enhanced counterpart $\hat{\mathbf{x}} = G_\theta(\mathbf{x})$, we use their soft segmentation maps (i.e., sigmoid outputs) and the corresponding soft skeletons to regularize global shape and connectivity. The red box highlights regions where noise affects the results, and the green box illustrates the order of skeletonization sequence. As the step index i increases, centerlines of progressively thicker vessels are extracted. See Sec. 4.2 for details.

boundaries. This representation is inherently more robust to blur, low contrast, and label jitter that commonly corrupt full masks and exist in noisy images. Even when masks are imperfect, their induced skeletons offer a reliable topological prior for morphology preservation during enhancement (see Fig. 2). However, the differentiability present to be a practical caveat, considering the hard skeletonization is non-differentiable.

Soft-Skeletonization [16] provide a solution, which approximate morphological skeleton on a probability mask using min and max pooling. Specifically, given the current map R_i (e.g., $R_0 := S(\mathbf{x})$) and $E_i = \text{minpool}(R_i)$ as the soft erosion process in step i . The algorithm will compute the opening O_i such that $O_i := \text{maxpool}(E_i)$. Then, the i -step soft skeleton layer $SK_i := \text{ReLU}(R_i - O_i)$ captures the centerline remnants at that radius. Intuitively, as shown in Fig. 2, each erosion step shrinks the local vessel radius, and the following opening regrows smooth interior regions. As a result, only vessel regions that are thick enough at depth i survive, with the remaining structure (i.e., SK_i) constitutes the per-depth skeleton layer (i.e., the centers of maximal inscribed disks). As the process continues, layers corresponding to progressively thicker vessels are extracted. (shown in green box in Fig. 2). Naturally, the final skeleton SK is the union of all per-depth layers, denoted as $SK(S(\mathbf{x})) := \bigcup_{i=0}^k SK_i$. Here, k represent the hyperparameter of total iteration steps.

Because we apply soft segmentation $S(\cdot)$ and compose only differentiable pooling operations and ReLU activation, the resulting soft skeleton $SK(\cdot)$ is naturally differentiable. We then define the skeleton-guided global topology preser-

vation regularization (SGA) as:

$$C_s := 1 - \frac{2 \times T_p(SK(S(\hat{\mathbf{x}})), S(\mathbf{x})) \times T_s(SK(S(\mathbf{x})), S(\hat{\mathbf{x}}))}{T_p(SK(S(\hat{\mathbf{x}})), S(\mathbf{x})) + T_s(SK(S(\mathbf{x})), S(\hat{\mathbf{x}}))}$$

where

$$\begin{cases} T_p = \frac{\sum (SK(S(\hat{\mathbf{x}})) \odot S(\mathbf{x})) + \epsilon}{\sum SK(S(\hat{\mathbf{x}})) + \epsilon} \\ T_s = \frac{\sum (SK(S(\mathbf{x})) \odot S(\hat{\mathbf{x}})) + \epsilon}{\sum SK(S(\mathbf{x})) + \epsilon} \end{cases} \quad (3)$$

Here T_p asks whether predicted centerlines lie inside high-probability input vessel regions, T_s checks whether the prediction covers the input's centerlines, ϵ ensures numerical stability and \odot works as element-wise production. Minimizing this loss penalizes spurious centerlines and gaps in prediction, which promotes preservation of overall vessel shape and connectivity [16].

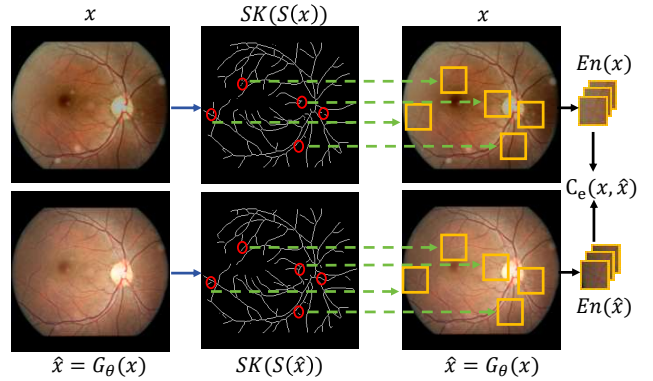


Figure 3. Illustration of the EVP module. Red circles mark vessel endpoints derived from the vessel skeleton, yellow boxes show the endpoint-centered windows in image space, and green dashed arrows indicate their correspondences. The local morphology regularization C_e is computed over these batches of small, endpoint-centered windows. We denote this extraction-and-windowing operator by $En(\cdot)$. For simplicity, we overload the skeletonization notation $SK(\cdot)$ to denote a hard, binary skeleton. See Sec. 4.3 for details.

4.3. Local Vascular Integrity via Endpoint Priors

Preserving vascular structure with a global, skeleton-based regularizer alone is not sufficient. Local topological changes (e.g., endpoint creation or loss) require additional attention. Given a low-quality image \mathbf{x} , we obtain its skeleton $SK(S(\mathbf{x}))$. For endpoint detection, we intentionally use a hard, binary skeleton and we overload $SK(\cdot)$ and $S(\cdot)$ to denote binarized operators here for simplicity.

Based on binary skeletonization, endpoints can be localized with a simple neighborhood count through all-ones 3×3 convolution kernel. Specifically, for each skeleton pixel, we count the number of skeleton pixels in its 8-connected neighborhood, and the endpoints are those pix-

els whose result is 1 (e.g., endpoints in marginal vessel branches or breaks) or 0 (e.g., the isolated points) besides the pixel itself. As illustrated in Fig. 3, red circles mark endpoint differences that arise after enhancement. In practice, such endpoint shifts typically occur in three regions: (i) peripheral, very thin branches, (ii) areas affected by image noise or artifacts, and (iii) neighborhoods of major anatomical structures (e.g., the optic disc), where brightness and texture can perturb segmentation and skeletonization. However, directly evaluating endpoints is challenging because they are represented as single-pixel, binary locations in skeleton. Moreover, unlike segmentation tasks that typically provide dense ground-truth masks, endpoint shifts observed in the enhancement setting may legitimately arise from artifact removal (as in Fig. 3) and should sometimes be treated as correct behavior rather than errors. Therefore, endpoint-based local structure preservation requires careful design.

Our approach, named EVP, is intuitive: rather than comparing endpoints directly, we regularize local structure within small windows centered at detected endpoints. In this setup, endpoints act only as anchors to localize regions that warrant additional attention. As shown in Fig. 3, when an endpoint is selected (red circle), we extract an $l \times l$ square window centered at that location in both the low-quality image \mathbf{x} and its enhanced counterpart $\hat{\mathbf{x}}$. Let M denote the set of those endpoint with $m := |M|$, and define $En_j(\cdot)$ represent the operation that crops the j -th endpoint-centered window. Then our endpoint-aware local regularizer defined as:

$$C_e(\mathbf{x}, \hat{\mathbf{x}}) := \frac{1}{m} \sum_{j=1}^m C(En_j(\mathbf{x}), En_j(\hat{\mathbf{x}})) \quad (4)$$

where C is an SSIM-based loss, designed to preserve local perceptual structure, and Eq. 4 can be easily implemented to batch of images. Our design bring three advantages. First, this formulation avoids brittle, one-pixel endpoint matching. Second, regardless of whether an endpoint appears to shift due to artifact or denoising, the model is always encouraged to maintain coherent local morphology around those locations, which susceptible to structure changes. Finally, because the loss is applied to image patches, it remains differentiable with respect to the generated image. We use the algorithms outlined in [23] to organize the endpoints selection.

4.4. Main learning Objective

Training VAOT has two phases. As shown in Fig. 4, Phase 1 trains for T_1 epochs with the OT-based adversarial objective (i.e., Eq. 2) to learn distribution transport while avoiding unnecessary changes on clean images. Phase 2 adds the SGA and EVP regularizers to preserve global morphology and local structure, and continues training for T_2

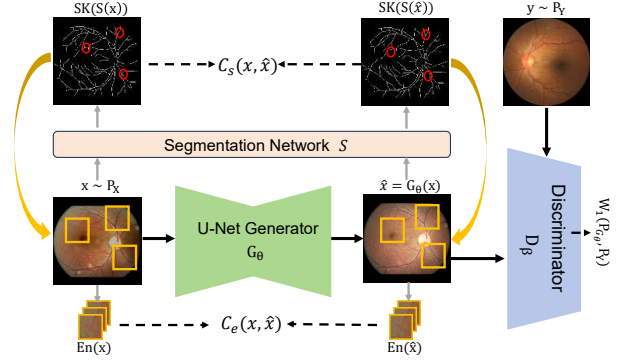


Figure 4. Illustration of the VAOT pipeline. The operator $SK(\cdot)$ denotes skeletonization, which is soft in Phase 1 and hard in Phase 2. Red circles mark detected endpoints and yellow arrows indicate the corresponding endpoint-centered local windows in image space. See Sec. 4.4 for details.

epochs with:

$$\max_{G_\theta} \min_{D_\beta} \lambda_1 \mathbb{E}_{\mathbf{x}}[C(\mathbf{x}, G_\theta(\mathbf{x}))] + \lambda_s \mathbb{E}_{\mathbf{x}}[C_s(\mathbf{x}, G_\theta(\mathbf{x}))] + \lambda_e \mathbb{E}_{\mathbf{x}}[C_e(\mathbf{x}, G_\theta(\mathbf{x}))] + \mathbf{W}_1(\mathbb{P}_{G_\theta(\mathbf{x})}, \mathbb{P}_{\mathbf{Y}}) \quad (5)$$

Here, λ_s and λ_e balance the topology terms. C denotes the base cost function, C_s is the skeleton-guided global topology term (i.e., Eq. 3), and C_e is the endpoint-aware local regularizer (i.e., Eq. 4).

5. Experiments

5.1. Experiment Setup

Tasks, Baselines and Metrics. We evaluate VAOT from four aspects: (i) Main enhancement to assess denoising performance; (ii) Cross-dataset evaluation to assess generalization ability; (iii) Downstream vessel segmentation to assess preservation of vascular morphology after enhancement; and (iv) Downstream Exudates (EX) and Hemorrhages (HE) lesion segmentation to assess retention of fine, high-frequency details post-enhancement.

We compare our method with the baselines in [26], including *paired algorithms*: SCR-Net [9], cofe-Net [15], PCE-Net [12], GFE-Net [11], RFormer [3]; *unpaired algorithms*: CycleGAN [25], OTT-GAN [21], OTRE-GAN [31], WGAN [1], Context-aware OT [20] and CUNSB-RFIE [4]. In the main enhancement task, we utilize Structural Similarity Measure (SSIM) and Peak Signal-to-Noise Ratio (PSNR) as evaluation metrics. For the downstream vessel segmentation task, we assess performance using Area under the ROC Curve (AUC), Area under the Precision-Recall Curve (PR), F1-score and Specificity (SP). In lesion segmentation task, we use AUC, PR

Table 1. Performance comparison of denoising evaluation in Full-Reference quality assessment experiments. The best performance in each column is highlighted in bold, with the second-best underlined.

	Method	EyeQ		IDRID		DRIVE	
		SSIM \uparrow	PSNR \uparrow	SSIM \uparrow	PSNR \uparrow	SSIM \uparrow	PSNR \uparrow
<i>Paired Methods</i>	SCR-Net [9]	0.9606	29.698	0.6425	18.920	0.6824	23.280
	Cofe-Net [15]	0.9408	24.907	0.7397	20.058	0.6671	21.774
	PCE-Net [12]	0.9487	29.895	<u>0.7764</u>	<u>23.201</u>	0.6704	24.041
	GFE-Net [11]	<u>0.9554</u>	<u>29.719</u>	0.7935	25.012	<u>0.6793</u>	<u>23.786</u>
	RFormer [3]	0.9260	27.163	0.5963	18.433	0.6311	22.172
<i>Unpaired Methods</i>	CycleGAN [25]	0.9313	<u>25.076</u>	0.7668	<u>22.511</u>	<u>0.6681</u>	22.686
	WGAN [7]	0.9266	<u>24.793</u>	0.7316	<u>21.325</u>	0.6431	20.408
	OTTGAN [21]	0.9275	24.065	0.7509	22.131	0.6635	21.938
	OTEGAN [32]	<u>0.9392</u>	24.812	0.7624	22.272	0.6642	22.183
	Context-aware OT [20]	0.9144	24.088	0.7338	21.790	0.6407	21.389
	CUNSB-RFIE [4]	0.9121	24.242	<u>0.7651</u>	22.448	0.6659	<u>22.510</u>
	VAOT(ours)	0.9433	25.253	0.7674	22.793	0.6701	22.287

Table 2. Performance comparison of vessel and lesion (EX and HE) segmentation in main enhancement task. In both paired and unpaired algorithms, the best performance in each column is highlighted in bold, with the second-best underlined.

Method	Vessel Segmentation				EX			HE		
	AUC \uparrow	PR \uparrow	F1 Score \uparrow	SP \uparrow	AUC	PR	F1 Score	AUC	PR	F1 Score
SCR-Net [9]	0.9227	0.7783	0.7000	0.9787	0.9683	0.6041	0.5556	0.9377	0.3213	0.3725
cofe-Net [15]	<u>0.9188</u>	<u>0.7698</u>	0.6895	0.9801	0.9623	0.5620	0.5349	0.9302	0.3152	0.3281
PCE-Net [12]	0.9146	0.7616	0.6790	0.9814	<u>0.9667</u>	<u>0.5876</u>	0.5066	<u>0.9545</u>	<u>0.3639</u>	<u>0.3736</u>
GFE-Net [11]	0.9175	0.7669	0.6832	0.9814	0.9560	0.5548	<u>0.5380</u>	0.9577	0.4113	0.3751
RFormer [3]	0.8990	0.7239	0.6374	<u>0.9806</u>	0.9626	0.5593	0.4692	0.9207	0.2677	0.3136
CycleGAN [25]	0.9015	0.7278	0.6462	0.9801	0.9447	0.4843	0.4790	0.8970	0.1624	0.2227
WGAN [7]	0.9081	0.7494	0.6768	0.9764	0.9522	0.4942	0.4859	0.8990	0.1847	0.2476
OTTGAN [21]	0.9034	0.7400	0.6609	0.9812	0.9492	0.4214	0.4365	0.8179	0.1448	0.2233
OTEGAN [32]	0.9156	<u>0.7678</u>	<u>0.6919</u>	0.9797	0.9562	<u>0.5191</u>	<u>0.4868</u>	0.9359	0.2800	<u>0.3165</u>
Context-aware OT [20]	0.8871	0.7077	0.6377	0.9791	0.9305	0.3318	0.3707	0.8091	0.0646	0.1184
CUNSB-RFIE [4]	<u>0.9163</u>	0.7626	0.6872	0.9784	<u>0.9572</u>	0.5381	0.4883	0.8488	0.1489	0.1893
VAOT(Ours)	0.9184	0.7742	0.6966	<u>0.9811</u>	0.9608	0.5043	0.4595	<u>0.9256</u>	<u>0.2680</u>	0.3280

and F1-score as metrics. For all experiments, we follow the implementation proposed in [26] for fair comparison.

Dataset. For the main enhancement task, we use the EyeQ dataset. Following the degradation pipeline in [15], we synthesize degraded inputs by combining spot artifacts, illumination perturbations, and blur. The dataset contains 5000 training images, 600 validation images, and 6217 test images. For paired methods, we organize the training set as aligned low-high image pairs. For unpaired methods, the low-quality images are generated from an additional set of 5000 retinal images disjoint from the high-quality set. For downstream evaluation, we use DRIVE [17] for vessel segmentation and IDRiD [14] for lesion segmentation.

VAOT setting. Our backbone follow the design outlined in [31, 32], and the pretrained vessel segmentation net-

work used to produce soft probability maps follows [24]. Training uses two phases of $T_1 = T_2 = 100$ epochs. At the start of each phase, the learning rate is reset to 1×10^{-4} and scheduled with cosine annealing. For soft-skeletonization we use $k = 20$ iterations and a numerical stabilizer $\epsilon = 1 \times 10^{-3}$. Additionally, we set the local window size to be 64 for our EVP module. For loss weight, we set $\lambda_1 = 30, \lambda_2 = 15, \lambda_s = 1, \lambda_e = 35$.

5.2. Experiment Results

Main Enhancement Tasks. Among all unpaired algorithms, VAOT demonstrates superior performance on the main enhancement task and in cross-dataset generalization on IDRiD and DRIVE. We train on EyeQ and apply the resulting model without adaptation to enhance low-quality

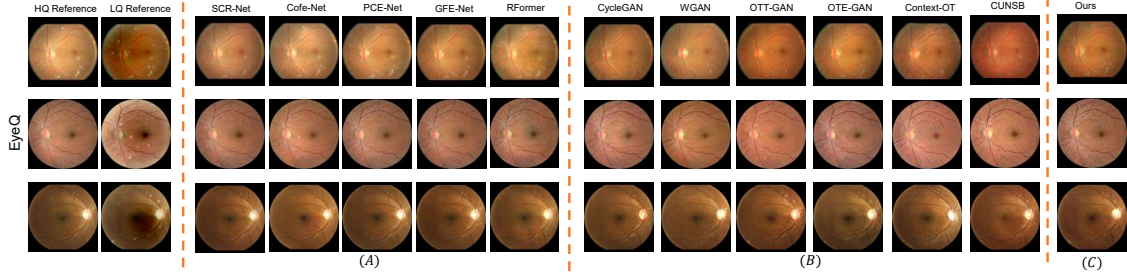


Figure 5. Illustration of main enhancement task over EyeQ. The first two columns represent low-high quality image pairs. Column (A) illustrates results from paired algorithms, column (B) shows results from unpaired algorithms, and column (C) shows our results (i.e., VAOT). See Sec. 5.2 for details.

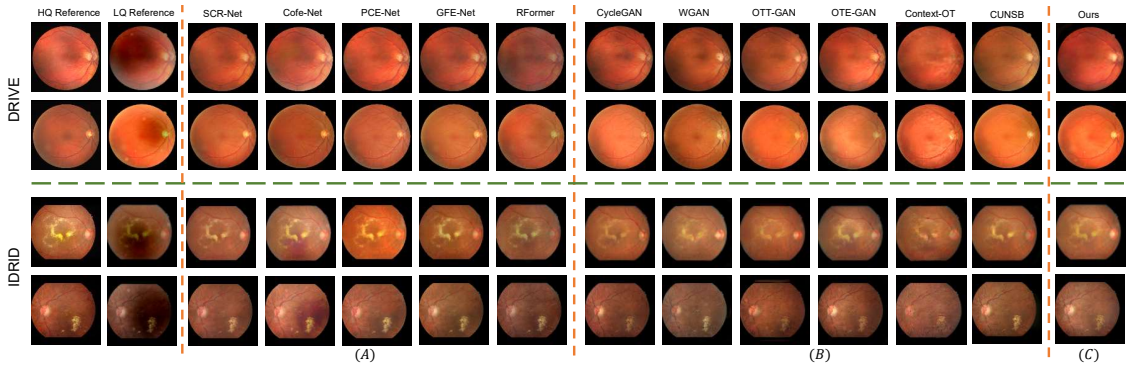


Figure 6. Illustration of generalization evaluation over IDRiD and DRIVE. The enhanced images are generated based on the best weight over EyeQ. The first two columns represent low-high quality image pairs. Column (A) illustrates results from paired algorithms, column (B) shows results from unpaired algorithms, and column (C) shows our results (i.e., VAOT). See Sec. 5.2 for details.

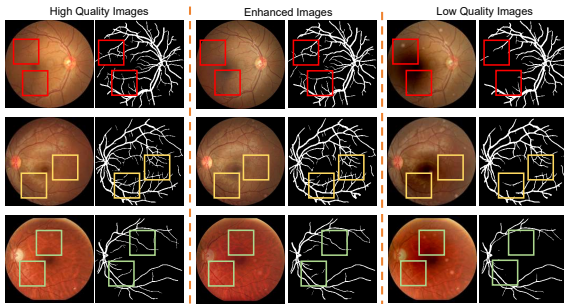


Figure 7. Illustration of high-quality, low-quality, and enhanced fundus images on EyeQ test set. Corresponding vessel-segmentation maps are shown alongside, generated using the model of [24]. Red, yellow, and green boxes highlight salient differences in vessel topology. See Sec. 5.2 for details.

images synthesized with the same degradation pipeline on IDRiD and DRIVE. As shown in Tab. 1, VAOT achieve the best SSIM (0.9433) and PSNR (25.253) over EyeQ, the highest SSIM and PSNR on IDRiD and the highest SSIM on DRIVE. Representative visual comparisons are shown in Fig. 5 (EyeQ) and Fig. 6 (IDRiD and DRIVE), which qualitatively corroborate the quantitative gains.

To evaluate whether our SGA and EVP designs help vascular structure preservation, we further analysis the vessel segmentation results from low-quality inputs, high-quality references and VAOT outputs. As shown in Fig. 7, the low-quality images exhibit broken branches and artifact-induced distortion (see red, yellow and green boxes), whereas VAOT restores branch continuity and global vascular shape to closely math the high-quality references. Mechanistically, the SGA term acts as a light global constraint that stabilizes connectivity and coarse geometry based on skeleton, while the EVP term applies an endpoint-based local window in image space to further refine fine structures near terminals. Importantly, since VAOT avoids hard morphology matching to degraded inputs, this topology guidance does not undermine denoising performance (see Tab. 1).

Although paired methods can yield higher absolute scores in Tab. 1, this does not diminish our contribution. In real clinical workflows, collecting perfectly aligned low/high-quality pairs is rarely feasible, making unpaired learning the more realistic setting. We therefore report paired baselines for context and completeness, while emphasizing the practical value of our unpaired approach.

Vessel and Lesion Segmentation. Downstream vessel seg-

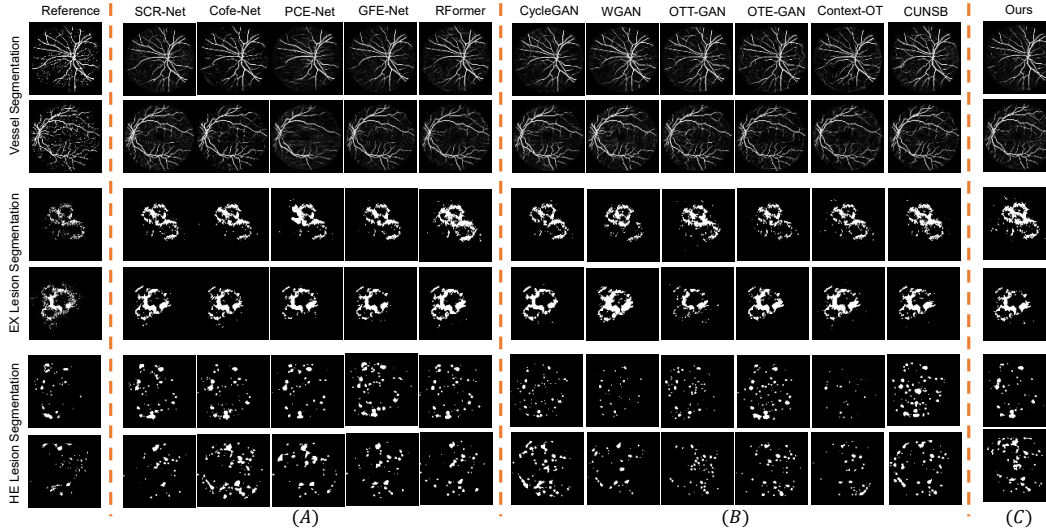


Figure 8. Illustration of vessel and lesion (i.e., EX and HE) segmentation results over DRIVE and IDRID, respectively. The first columns represent ground truth mask. Column (A) illustrates results from paired algorithms, column (B) shows results from unpaired algorithms, and column (C) shows our results (i.e., VAOT). See Sec. 5.2 for details.

mentation results further demonstrate effective preservation of vascular morphology. As reported in Tab. 2, VAOT achieves the best AUC, PR, and F1 scores, and the second-best SP score among the seven unpaired methods. Qualitative examples in Fig. 8 corroborate these findings: several unpaired baselines (e.g., CycleGAN, OTT-GAN) introduce artifacts that lead to false-positive vessel predictions or missed peripheral loops, whereas VAOT maintains coherent branching and continuity.

For lesion segmentation (i.e., EX and HE lesion segmentation), VAOT, despite emphasizing vascular structure, still retains strong performance on these higher-frequency details. As shown in Tab. 2, it attains the best AUC on EX and the best F1 score on HE, indicating competitive preservation of fine-grained lesion structure.

Method	SGA	EVP	SSIM \uparrow	PSNR \uparrow
OTEGAN	×	×	0.9392	24.812
Ours (VAOT)	✓	×	0.9406	24.967
	✓	✓	0.9433	25.253

Table 3. Ablation Study of SGA and EVP structures. Specifically, OTEGAN denotes the backbone without any vessel-aware modules. Adding SGA and EVP progressively improves denoising (e.g., PSNR/SSIM), indicating their orthogonal effects. See Sec. 5.3 for details.

5.3. Ablation Study

In VAOT, we introduce two structure-aware components to better preserve vascular anatomy during retinal fundus enhancement. Specifically, the SGA regularizer promotes

global vessel-skeleton alignment, while the EVP regularizer encourages local consistency around detected endpoints. We assess their individual contributions with an ablation study on the same test set used for the main enhancement task. As shown in Tab. 3, adding SGA to the backbone (i.e., OTEGAN) yields modest gains in SSIM and PSNR. Adding EVP on top of SGA produces larger improvements, increasing SSIM from 0.9406 to 0.9433 and PSNR from 24.967 to 25.253, indicating that the two regularizers provide complementary benefits. Unless otherwise noted, all hyperparameters match those of the main experiments.

A natural question is why SGA alone offers only marginal improvements. We attribute this to a deliberately conservative weight $\lambda_s = 1$ used across all experiments. Because exact skeleton alignment, can be brittle under noisy inputs, we position SGA as a gentle prior that biases the solution toward preserving global vessel morphology without enforcing exact, potentially unsafe matches. By contrast, the EVP regularizer delivers larger improvements because it directly targets local discontinuities around detected endpoints, no matter those endpoints arise from denoising gaps or imaging artifacts. As a result, it could strengthening local morphology and connectivity.

6. Conclusion

In this work, we present VAOT, a vessel-aware optimal transport framework for unpaired retinal fundus image enhancement. To preserve global vascular morphology, we introduce a skeleton guided morphology alignment regularizer. To maintain local vascular integrity, including connectivity and small loop consistency, we introduce a regular-

izer guided by detected endpoints and applied within local windows. Extensive experiments demonstrate that VAOT is effective and generalizes well for the primary enhancement task and across datasets. Moreover, VAOT better preserves vascular structure, as evidenced by improved performance in downstream vessel segmentation. We believe these findings advance structure preserving enhancement of unpaired fundus images and provide a useful foundation for future research.

References

- [1] Martin Arjovsky, Soumith Chintala, and Léon Bottou. Wasserstein generative adversarial networks. In *International conference on machine learning*, pages 214–223. PMLR, 2017. [2](#), [5](#)
- [2] Dominique Brunet, Edward R Vrscay, and Zhou Wang. On the mathematical properties of the structural similarity index. *IEEE Transactions on Image Processing*, 21(4):1488–1499, 2011. [3](#)
- [3] Zhuo Deng, Yuanhao Cai, Lu Chen, Zheng Gong, Qiqi Bao, Xue Yao, Dong Fang, Wenming Yang, Shaohong Zhang, and Lan Ma. Rformer: Transformer-based generative adversarial network for real fundus image restoration on a new clinical benchmark. *IEEE Journal of Biomedical and Health Informatics*, 26(9):4645–4655, 2022. [5](#), [6](#)
- [4] Xuanzhao Dong, Vamsi Krishna Vasa, Wenhui Zhu, Peijie Qiu, Xiwen Chen, Yi Su, Yujian Xiong, Zhangsihao Yang, Yanxi Chen, and Yalin Wang. Cunsb-rfie: Context-aware unpaired neural schr"o} dinger bridge in retinal fundus image enhancement. *arXiv preprint arXiv:2409.10966*, 2024. [1](#), [2](#), [5](#), [6](#)
- [5] Oana M. Dumitrascu, Xin Li, Wenhui Zhu, Bryan K. Woodruff, Simona Nikolova, Jacob Sobczak, Amal Youssef, Siddhant Saxena, Janine Andreev, Richard J. Caselli, John J. Chen, and Yalin Wang. Color fundus photography and deep learning applications in alzheimer's disease. *Mayo Clinic Proceedings: Digital Health*, 2024. [1](#)
- [6] Oana M Dumitrascu, Xin Li, Wenhui Zhu, Bryan K Woodruff, Simona Nikolova, Jacob Sobczak, Amal Youssef, Siddhant Saxena, Janine Andreev, Richard J Caselli, et al. Color fundus photography and deep learning applications in alzheimer disease. *Mayo Clinic Proceedings: Digital Health*, 2(4):548–558, 2024. [1](#)
- [7] Ishaan Gulrajani, Faruk Ahmed, Martin Arjovsky, Vincent Dumoulin, and Aaron C Courville. Improved training of wasserstein gans. *Advances in neural information processing systems*, 30, 2017. [2](#), [3](#), [6](#)
- [8] Xiaoling Hu, Fuxin Li, Dimitris Samaras, and Chao Chen. Topology-preserving deep image segmentation. *Advances in neural information processing systems*, 32, 2019. [2](#)
- [9] Heng Li, Haofeng Liu, Huazhu Fu, Hai Shu, Yitian Zhao, Xiaoling Luo, Yan Hu, and Jiang Liu. Structure-consistent restoration network for cataract fundus image enhancement. In *International Conference on Medical Image Computing and Computer-Assisted Intervention*, pages 487–496. Springer, 2022. [5](#), [6](#)
- [10] Heng Li, Haofeng Liu, Huazhu Fu, Hai Shu, Yitian Zhao, Xiaoling Luo, Yan Hu, and Jiang Liu. Structure-consistent restoration network for cataract fundus image enhancement. In Linwei Wang, Qi Dou, P. Thomas Fletcher, Stefanie Speidel, and Shuo Li, editors, *Medical Image Computing and Computer Assisted Intervention – MICCAI 2022*, pages 487–496, Cham, 2022. Springer Nature Switzerland. [2](#)
- [11] Heng Li, Haofeng Liu, Huazhu Fu, Yanwu Xu, Hai Shu, Ke Niu, Yan Hu, and Jiang Liu. A generic fundus image enhancement network boosted by frequency self-supervised representation learning. *Medical Image Analysis*, 90:102945, 2023. [2](#), [5](#), [6](#)
- [12] Haofeng Liu, Heng Li, Huazhu Fu, Ruoxiu Xiao, Yunshu Gao, Yan Hu, and Jiang Liu. Degradation-invariant enhancement of fundus images via pyramid constraint network. In Linwei Wang, Qi Dou, P. Thomas Fletcher, Stefanie Speidel, and Shuo Li, editors, *Medical Image Computing and Computer Assisted Intervention – MICCAI 2022*, pages 507–516, Cham, 2022. Springer Nature Switzerland. [2](#), [5](#), [6](#)
- [13] Roey Mechrez, Itamar Talmi, and Lihl Zelnik-Manor. The contextual loss for image transformation with non-aligned data, 2018. [2](#)
- [14] Prasanna Porwal and et al. Idrid: A database for diabetic retinopathy screening research. *Data*, 3(3), 2018. [6](#)
- [15] Ziyi Shen, Huazhu Fu, Jianbing Shen, and Ling Shao. Modeling and enhancing low-quality retinal fundus images. *IEEE transactions on medical imaging*, 40(3):996–1006, 2020. [5](#), [6](#)
- [16] Suprosanna Shit, Johannes C Paetzold, Anjany Sekuboyina, Ivan Ezhov, Alexander Unger, Andrey Zhylyka, Josien PW Pluim, Ulrich Bauer, and Bjoern H Menze. cldice-a novel topology-preserving loss function for tubular structure segmentation. In *Proceedings of the IEEE/CVF conference on computer vision and pattern recognition*, pages 16560–16569, 2021. [4](#)
- [17] J. Staal, M.D. Abramoff, M. Niemeijer, M.A. Viergever, and B. van Ginneken. Ridge-based vessel segmentation in color images of the retina. *IEEE Transactions on Medical Imaging*, 23(4):501–509, 2004. [6](#)
- [18] Yubo Tan, Kai-Fu Yang, Shi-Xuan Zhao, and Yong-Jie Li. Retinal vessel segmentation with skeletal prior and contrastive loss. *IEEE Transactions on Medical Imaging*, 41(9):2238–2251, 2022. [2](#)
- [19] Stefan Van der Walt, Johannes L Schönberger, Juan Nunez-Iglesias, François Boulogne, Joshua D Warner, Neil Yager, Emmanuelle Gouillart, and Tony Yu. scikit-image: image processing in python. *PeerJ*, 2:e453, 2014. [2](#)
- [20] Vamsi Krishna Vasa, Peijie Qiu, Wenhui Zhu, Yujian Xiong, Oana Dumitrascu, and Yalin Wang. Context-aware optimal transport learning for retinal fundus image enhancement. *arXiv preprint arXiv:2409.07862*, 2024. [1](#), [2](#), [5](#), [6](#)
- [21] Wei Wang, Fei Wen, Zeyu Yan, and Peilin Liu. Optimal transport for unsupervised denoising learning. *IEEE Transactions on Pattern Analysis and Machine Intelligence*, 45(2):2104–2118, 2022. [1](#), [3](#), [5](#), [6](#)
- [22] Zhou Wang, Eero P Simoncelli, and Alan C Bovik. Multi-scale structural similarity for image quality assessment. In

The Thirty-Seventh Asilomar Conference on Signals, Systems & Computers, 2003, volume 2, pages 1398–1402. Ieee, 2003. [3](#)

- [23] Feixiang Zhou, Zhuangzhi Gao, He Zhao, Jianyang Xie, Yanda Meng, Yitian Zhao, Gregory YH Lip, and Yalin Zheng. Glcp: Global-to-local connectivity preservation for tubular structure segmentation. *arXiv preprint arXiv:2507.21328*, 2025. [5](#)
- [24] Yuqian Zhou, Hanchao Yu, and Humphrey Shi. Study group learning: Improving retinal vessel segmentation trained with noisy labels. In *Medical Image Computing and Computer Assisted Intervention–MICCAI 2021: 24th International Conference, Strasbourg, France, September 27–October 1, 2021, Proceedings, Part I 24*, pages 57–67. Springer, 2021. [2](#), [6](#), [7](#)
- [25] Jun-Yan Zhu, Taesung Park, Phillip Isola, and Alexei A Efros. Unpaired image-to-image translation using cycle-consistent adversarial networks. In *Proceedings of the IEEE international conference on computer vision*, pages 2223–2232, 2017. [1](#), [2](#), [5](#), [6](#)
- [26] Wenhui Zhu, Xuanzhao Dong, Xin Li, Yujian Xiong, Xiwen Chen, Peijie Qiu, Vamsi Krishna Vasa, Zhangsihao Yang, Yi Su, Oana Dumitrascu, et al. Eyebench: A call for more rigorous evaluation of retinal image enhancement. *arXiv preprint arXiv:2502.14260*, 2025. [2](#), [5](#), [6](#)
- [27] Wenhui Zhu, Xin Li, Xiwen Chen, Peijie Qiu, Vamsi Krishna Vasa, Xuanzhao Dong, Yanxi Chen, Natasha Lepore, Oana Dumitrascu, Yi Su, et al. Retinalgpt: A retinal clinical preference conversational assistant powered by large vision-language models. *arXiv preprint arXiv:2503.03987*, 2025. [1](#)
- [28] Wenhui Zhu, Peijie Qiu, Xiwen Chen, Huayu Li, Hao Wang, Natasha Lepore, Oana M Dumitrascu, and Yalin Wang. Beyond mobilenet: An improved mobilenet for retinal diseases. In *International Conference on Medical Image Computing and Computer-Assisted Intervention*, pages 56–65. Springer, 2023. [1](#)
- [29] Wenhui Zhu, Peijie Qiu, Xiwen Chen, Xin Li, Natasha Lepore, Oana M. Dumitrascu, and Yalin Wang. nnmobilenet: Rethinking cnn for retinopathy research. In *Proceedings of the IEEE/CVF Conference on Computer Vision and Pattern Recognition (CVPR) Workshops*, pages 2285–2294, June 2024. [1](#)
- [30] Wenhui Zhu, Peijie Qiu, Xiwen Chen, Xin Li, Natasha Lepore, Oana M Dumitrascu, and Yalin Wang. nnmobilenet: rethinking cnn for retinopathy research. In *Proceedings of the IEEE/CVF Conference on Computer Vision and Pattern Recognition*, pages 2285–2294, 2024. [1](#)
- [31] Wenhui Zhu, Peijie Qiu, Oana M Dumitrascu, Jacob M Sobczak, Mohammad Farazi, Zhangsihao Yang, Keshav Nandakumar, and Yalin Wang. Otre: Where optimal transport guided unpaired image-to-image translation meets regularization by enhancing. In *International Conference on Information Processing in Medical Imaging*, pages 415–427. Springer, 2023. [1](#), [2](#), [3](#), [5](#), [6](#)
- [32] Wenhui Zhu, Peijie Qiu, Mohammad Farazi, Keshav Nandakumar, Oana M Dumitrascu, and Yalin Wang. Optimal

transport guided unsupervised learning for enhancing low-quality retinal images. *Proc IEEE Int Symp Biomed Imaging*, 2023. [1](#), [2](#), [3](#), [6](#)